# High-Resolution Imaging of the Ocean Surface Backscatter by Inversion of Altimeter Waveforms

JEAN TOURNADRE, BERTRAND CHAPRON, AND NICOLAS REUL

*Laboratoire d'Oceanographie Spatiale, IFREMER, Plouzane, France*

(Manuscript received 24 August 2010, in final form 4 April 2011)

ABSTRACT

This paper presents a new method to analyze high-resolution altimeter waveforms in terms of surface backscatter. Over the ocean, a basic assumption of modeling altimeter echo waveforms is to consider a homogeneous sea surface within the altimeter footprint that can be described by a mean backscatter coefficient. When the surface backscatter varies strongly at scales smaller than the altimeter footprint size, such as in the presence of surface slicks, rain, small islands, and altimeter echoes can be interpreted as high-resolution images of the surface whose geometry is annular and not rectangular. A method based on the computation of the imaging matrix and its pseudoinverse to infer the surface backscatter at high resolution (~300 m) from the measured waveforms is presented. The method is tested using synthetic waveforms for different surface backscatter fields and is shown to be unbiased and accurate. Several applications can be foreseen to refine the analysis of rain patterns, surface slicks, and lake surfaces. The authors choose here to focus on the small-scale variability of backscatter induced by a submerged reef smaller than the altimeter footprint as the function of tide, significant wave height, and wind.

## 1. Introduction

All satellite altimeters use pulse-limited geometry and a full deramp technique to measure the power backscatter by the ocean surface as a function of time [i.e., the altimeter pulse echo waveform; see, e.g., Chelton et al. (2001) for explanation on pulse-limited altimeters]. Over an ocean surface, the waveform has a characteristic shape that can be described analytically using in general the classical Brown model (Brown 1977). The altimeter geophysical parameters—epoch (range), surface backscatter, and significant wave height (swh) as well as the satellite off-nadir angle—are estimated by fitting the theoretical model to the measured waveforms. The basic assumption of the echo waveform models is that the distribution of sea surface roughness within the altimeter footprint is homogeneous and can be described with a mean value. However, previous studies such as Tournadre (1998), Quartly et al. (2001), or Tournadre et al. (2006) have shown that this basic hypothesis is not always valid, notably in the presence of rain, sea ice, small islands or reefs, surface slicks, or very low wind conditions.

Under such occurrences, an altimeter can be seen as an imager of the sea surface backscatter whose imaging process is more complex than a classical one in the sense that pixels are not rectangular but annular. The imaging process of the sea surface (i.e., the transform matrix between the real and the waveform spaces) depends only on the satellite and altimeter geometry and can be analytically computed. We present a method to invert the measured waveforms in terms of surface backscatter at a resolution on the order of the along-track 20-Hz resolution (290 m for Jason). The method is validated using simulated waveforms and is shown to be unbiased and to have an rms on the order of 0.25 dB. Several applications for which small-scale variability of backscatter is of interest can be envisioned, such as the fine analysis of rain patterns or surface slicks. We choose here to focus on the analysis of the change of roughness over a small submerged reef, which is still quite poorly documented (Hearn 1999).

## 2. Inversion of altimeter waveforms

### a. Altimetry principle

Satellite altimeters are nadir-looking radar that emit short pulses reflected by the sea surface and that

*Corresponding author address:* Jean Tournadre, Laboratoire d'Oceanographie Spatiale, IFREMER, BP 70 29280, Plouzane, France.
E-mail: jean.tournadre@ifremer.fr

DOI: 10.1175/2011JTECHO820.1

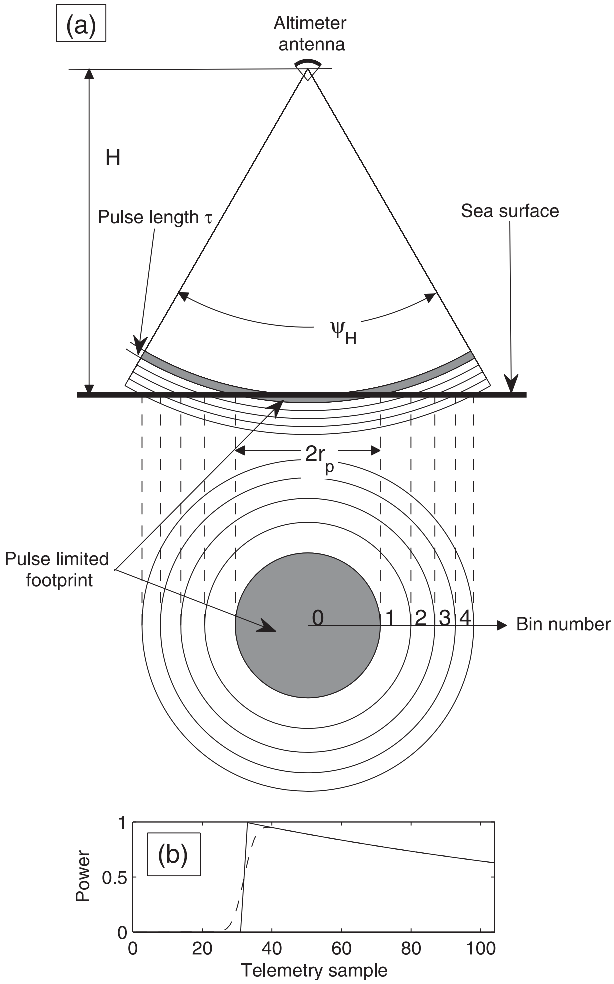


FIG. 1. (a) Geometry of a satelliteborne radar altimeter, where $H$ is the satellite altitude, $\psi_H$ the antenna half-beamwidth, $r_p$ the radius of the pulse-limited footprint, and $\tau$ the length of the pulse. (b) Examples of waveforms for a Jason-like altimeter for a flat sea (solid line) and a 5-m swh (dashed line).

measure the backscattered power as a function of time (the altimeter pulse echo waveform). Figure 1 shows a pulse being reflected from a flat surface. As the pulse advances, the illuminated area grows rapidly from a point to a disk, as does the returned power. Eventually, an annulus is formed and the geometry is such that the annulus area remains constant as the diameter increases. The returned signal strength, which depends on the reflecting area, grows rapidly until the annulus is formed and remains constant until the growing annulus reaches the edge of the radar beam, where it starts to diminish.

In an agitated sea, a change of the surface elevation larger than the pulse width causes the returned pulse to be distorted and stretched. The effect of this is to impose an additional slope on the leading edge of the returned signal strength curve (Fig. 1a). This slope is related to the ocean wave height and the midpoint of this leading edge slope is equivalent to the reflection from the average position of the surface (i.e., the mean sea surface). The amplitude of the waveform depends on the mean roughness over the altimeter footprint, which can be empirically related to wind speed.

Assuming that the distribution of the sea surface roughness and of the elevation are homogeneous over the altimeter footprint, the backscatter coefficient can be expressed as a convolution product of the radar point target response, the flat sea surface response, and the joint probability density function of slope and elevation of the sea surface (Brown 1977; Barrick and Lipa 1985).

Further, assuming a Gaussian shape of standard deviation $u_b$ for the antenna beam pattern $g$, a Gaussian shape of standard deviation $\sigma_\tau$ for the compressed altimeter pulse $P$, and also a Gaussian joint probability of sea surface slope and elevation $p_j$, under the small angle approximation, the cross section $\sigma$ simplifies to

$$\sigma(t) = \frac{\pi^2 H''|R(0)|^2\sigma_\tau\sigma_0}{2\sigma_p}\int_0^\infty e^{-u/u_b}e^{-(x-u)^2/2\sigma_p^2}\,du, \quad (1)$$

where $t$ is the time; $x = ct/2$ is the distance between the surface and the antenna; $u = (H'\psi^2)/2$ is the range; $H'$ and $H''$, defined by $H' = H(1 + H/a)$ and $H'' = H/(1 + H/a)$, are the reduced and extended satellite heights, $H$ being the satellite altitude, and $a$ the earth's radius; $R(0)$ is the Fresnel coefficient at zero incidence; $u_b$ is defined by $u_b = (H'\psi_b^2)/2$, with $\psi_b = \psi_H/\sqrt{8\ln 2}$, $\psi_H$ being the two-way half-power antenna beamwidth; $\sigma_p$ is defined by $\sigma_p = \sqrt{h^2 + \sigma_\tau^2}$; $h$ is the rms wave height; $\sigma_0$ is the mean surface backscatter coefficient defined as a function of the rms of the wave slopes ($s_x$ and $s_y$) in two orthogonal directions; and $\rho_{xy}$ is the correlation coefficient of the wave slopes along these two axes by

$$\sigma_0 = \frac{1}{2s_xs_y\sqrt{1-\rho_{xy}^2}}. \quad (2)$$

The first term within the integral represents the effect of the antenna pattern while the second term represents the effect of the variations of the surface elevation.

Equation (1) can be easily integrated and simplifies to the classical Brown model:

$$\sigma(t) = \frac{1}{2}(2\pi)^{3/2}H''\sigma_\tau\sigma_0\left[1 + \mathrm{erf}\left(\frac{x}{\sqrt{2}\sigma_p}\right)\right]e^{-x/u_b}. \quad (3)$$

It should be noted that $t = 0$ corresponds to the mean sea level. Examples of altimeter waveforms for a flat sea and a 5-m significant wave height are presented in Fig. 1.

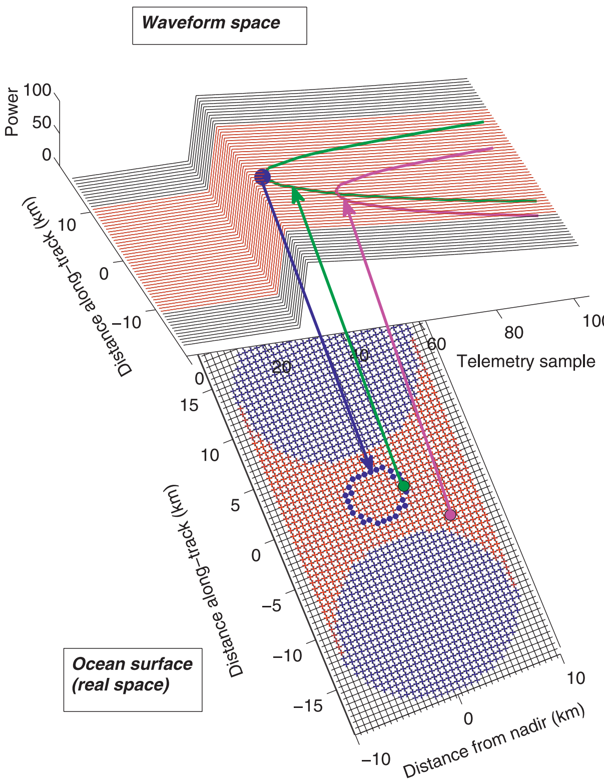


FIG. 2. Schematic representation of the altimeter imaging process. The lower plot presents the regular grid defined on the sea surface while the upper plot presents the waveform space. The green (magenta) parabola represents the ensemble of the waveform space bins to which the green (magenta) point of the surface contributes. The blue annulus in the real space represents the ensemble of surface elements that contribute to the blue bin of the waveform space. The group of red waveforms is the image of the ensemble of blue points of the sea surface. Within this ensemble, the red surface points are the ones that contribute only to the purple waveforms.

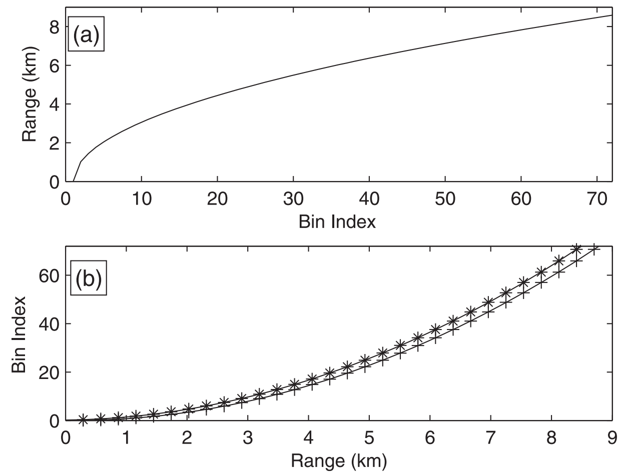


FIG. 3. (a) Range as a function of bin index for *Jason-1* and *-2* altimeters, and (b) minimum and maximum bin indices for a flat sea surface as a function of the distance from nadir of the gridcell element.

A main assumption of the Brown model is that the sea surface within the altimeter footprint can be represented by a mean surface backscatter $\sigma_0$. When the surface backscatter strongly varies at scales smaller than the altimeter footprint diameter, the waveform can significantly departs from the Brown model and Eq. (1) is not valid. In such cases, an altimeter can be seen as an imager of the sea surface backscatter whose pixels are annular (see Fig. 1) and not rectangular. The imaging principle of the sea surface by an altimeter is illustrated in Fig. 2. A point (bin) of the waveform space is associated with a disk (at nadir) or an annulus in real space (i.e., points with the same range). For example the blue bin of the waveform space in the figure is the image of the blue annulus in the real space. Reciprocally, a point in the real space contributes to an ensemble of bins in the waveform space, which is a parabola determined by the satellite orbit characteristics. For example, the green and magenta elements of the real surface contribute to the waveform bins along the green and magenta parabolas in the waveform space.

The ensemble of blue points in the real space contributes to the ensemble of red waveforms in the figure. But within this ensemble of surface points the subset represented in red represents the points that contribute only to the red waveforms. Because of the altimeter sampling geometry, two symmetrical points with respect to the satellite track have identical images leading to a left/right ambiguity.

Correspondingly, we can consider that the wave height is homogeneous over the altimeter footprint and that the surface backscatter is modulated by short-scale variations. Under this approximation the echo waveform becomes

$$\sigma_0(t) = \alpha \int_0^{2\pi} \int_0^{\infty} \sigma_s(u,\theta) e^{-u/u_b} e^{-(ct/2-u)^2/2\sigma_p^2}\, du\, d\theta, \quad (4)$$

where $\alpha = \pi^2 H'' |R(0)|^2 \sigma_\tau / 2\sigma_p$ is a normalization coefficient, $\theta$ is the azimuth, $u$ is the range, $c$ is the speed of light, and $\sigma_s$ is the surface backscatter.

### b. *Inversion method*

In practice, high-resolution (HR), altimeter-measured waveforms are given every 0.05 s (for the Jason satellites) or 0.056 s (for *Envisat*) in telemetry bins (gate) of width $\tau$ (length of the pulse). These HR waveforms are themselves an average of individual echoes (90 for Jason and 100 for *Envisat*) to reduce the speckle noise. It should also be noted that the Ocean Topography Experiment

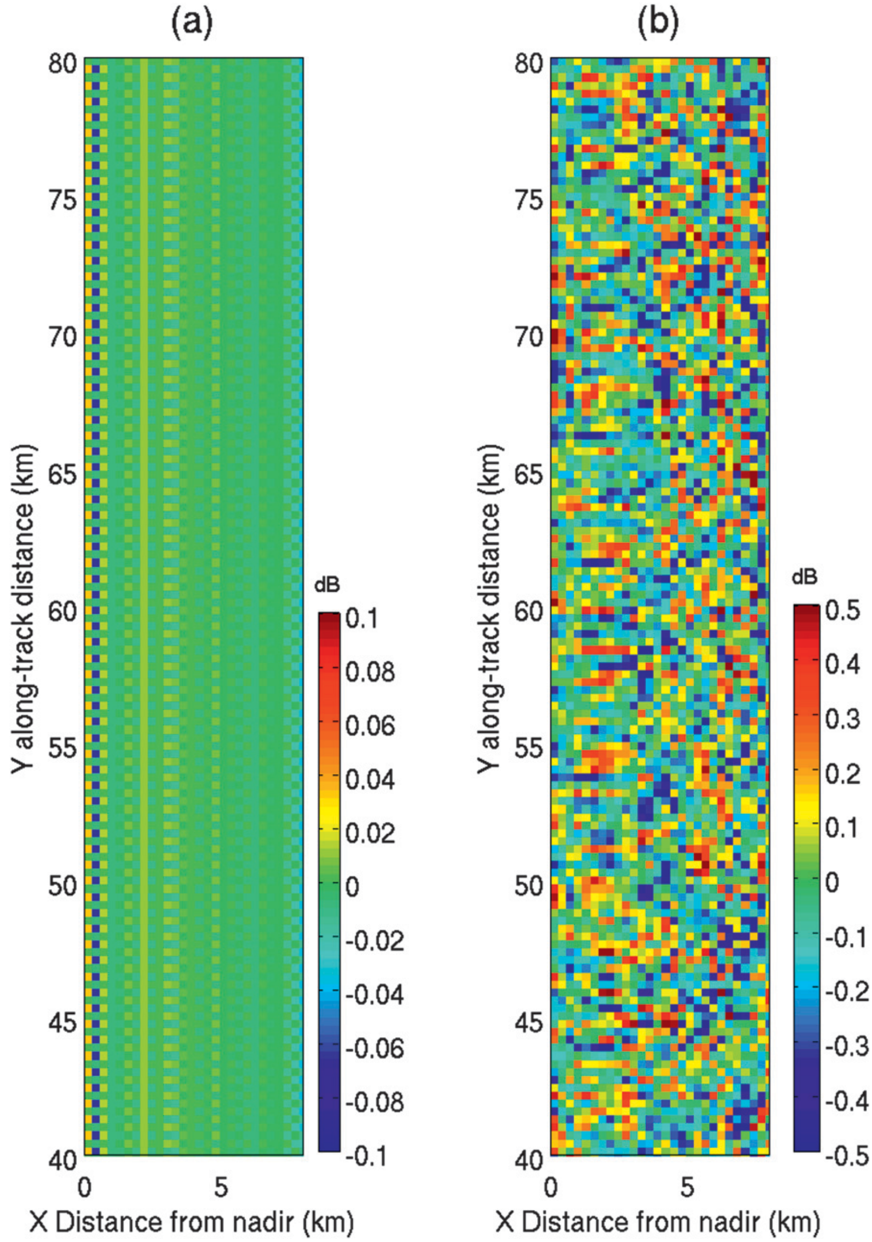


FIG. 4. Difference between the original and retrieved $\sigma_0$ for (a) the constant and (b) noisy cases.

(TOPEX) waveforms (available only every 0.1 s) whose original 128 telemetry bins have been irreversibly compressed to 64 cannot be used for inversion. The distance between two consecutive HR waveforms is 290 m for Jason and 340 m for *Envisat*. The total number of bins is 104 for Jason and 128 for *Envisat* and the nominal track point (i.e., the mean sea level or $t = 0$) is shifted to bin 32.5 for Jason and 47 for *Envisat*. For a flat sea, the range of the telemetry bins varies from about 1 km at bin 1 to about 8 km at bin 104 (see Fig. 3). The distance between two consecutive bins (i.e., the width of the annular pixel) varies from about 2 km at nadir (circular) to 60 m at bin 104. Hereafter, the portions of the waveform above the sea level (i.e., before the track point) are discarded, as they do not contain information on the surface backscatter.

Assuming that the surface backscatter is defined on a regular along-track grid $\{x_{kl}, y_{kl}\}$, and further assuming that the rms of the surface is small (low significant wave height), Eq. (4) can be discretized as follows: the $j$th element of the $i$th waveform $w_{ij}$ is the summation of

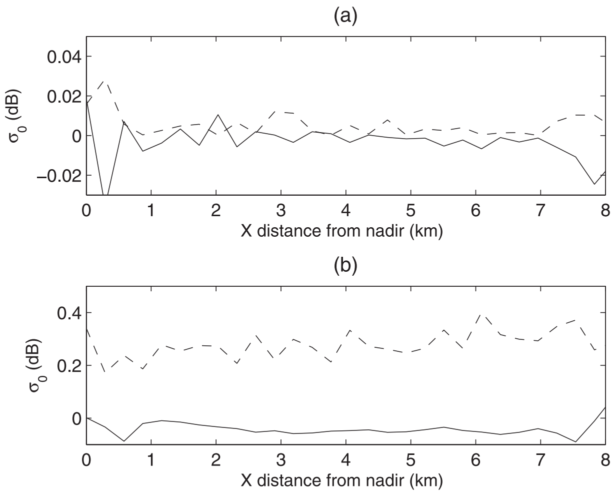


FIG. 5. Mean (solid line) and rms (dashed line) of the difference between the original and retrieved $\sigma_0$ for the (a) constant and (b) noisy $\sigma_0$ cases as a function of distance from nadir.

the surface backscatter elements $\sigma_{kl}$, whose range is between the range limits $\{u_j, u_{j+1}\}$ of bin $j$:

$$w_{ij} = \alpha \sum_k \sum_l a_{kl}\sigma_{kl}e^{-u(k,l)/u_b}\left[1 + \mathrm{erf}\left(\frac{u_j}{\sqrt{2}\sigma_p}\right)\right], \quad (5)$$

where the range $u_{kl}$ satisfies

$$u_j \le u_{kl} = \frac{(x_{kl} - x_i^0)^2 + (y_{kl} - y_i^0)^2}{H''c\tau} \le u_{j+1}, \quad (6)$$

where $\tau$ is the pulse length, $x$ and $y$ are the along- and across-track coordinates, $x_i^0$ and $y_i^0$ are the nadir coordinates corresponding to the $i$th waveform, and $a_{kl}$ is the surface of the intersection of the $\{k, l\}$ grid cell and the annulus of bin $j$. In a first-order approximation we assume all the $u_{kl}$ to be equal to $\overline{u_j} = (u_j + u_{j+1})/2$, thus Eq. (5) simplifies to

$$W_{ij} = w_{ij}\frac{e^{\overline{u_j}/u_b}}{\left[1 + \mathrm{erf}\left(\frac{\overline{u_j}}{\sqrt{2}\sigma_p}\right)\right]} = \alpha \sum_{k,l} a_{kl}\sigma_{kl}, \quad (7)$$

where $W$ represents the waveform detrended for the beamwidth by the term $e^{\overline{u_j}/u_b}$ and wave height effects by the term $[1 + \mathrm{erf}(\overline{u_j}/\sqrt{2}\sigma_p)]^{-1}$.

Equation (7) shows that the inversion of a single waveform in terms of surface backscatter is not possible. Let us consider a series of detrended waveform $\{W_i, i = 1, \ldots, N\}$ (in red in Fig. 2); they can be expressed in matrix form as

$$\mathbf{W} = \mathbf{A} \cdot \mathbf{S}, \quad (8)$$

where $\mathbf{S}$ is the matrix of the mean left/right surface backscatter (because of the left/right ambiguity) and $\mathbf{A}$ is the altimeter imaging matrix that depends only on the altimeter geometry and can be easily computed using the range Eq. (6).

Let $X_{ij}$ be a surface grid element of area $dx$, $dy$ centered on $x_{ij}$, $y_{ij}$ . The coefficient $a_{ijkl}$ of the imaging matrix $\mathbf{A}$ is equal to the surface of intersection between the grid element and the annulus centered at $x_0^k$, $y_0^k$ and radii $r_l$ and $r_{l+1}$ (i.e., the range of bin $l$):

$$a_{ijkl} = \int_{y_{ij}-dy/2}^{y_{ij}+dy/2} [f_1(y) - f_2(y)]\, dy, \quad (9)$$

where

$$f_1(y) = \min\left[\sqrt{r_{l+1}^2 - (y - y_0^k)^2},\, x_{ij} + \frac{dx}{2}\right] \quad (10)$$

$$f_2(y) = \max\left[\sqrt{r_l^2 - (y - y_0^k)^2},\, x_{ij} - \frac{dx}{2}\right], \quad (11)$$

where

$$r_l = \sqrt{lH''c\tau}. \quad (12)$$

The resolution of the surface backscatter grid has been chosen as the distance between two consecutive HR waveforms (290 m for Jason and 340 m for *Envisat*). The minimum number of waveforms to be considered is constrained by the width of the image of a nadir point in the waveform space that is about 3 s of data or 60 waveforms. In practice, $N$ has been fixed to 75. For such grids, the linear system of Eq. (8) is overdetermined and can be inverted using pseudo–Moore-Penrose inverse $\mathbf{A}^+$ computed using singular value decomposition (Penrose 1955):

$$\mathbf{S} = \mathbf{A}^+ \cdot \mathbf{W}. \quad (13)$$

For each altimeter 20-Hz waveform, the 75 surrounding waveforms are considered and the local $\mathbf{S}$ matrix is estimated using Eq. (13). Only the subset of points whose images are completely included in the waveforms are kept and the local matrices are then averaged to produce the final estimate of the along-track surface backscatter.

A main assumption of the inversion method is that the rms of the sea surface elevation is low, which is quite a strong constraint. However, higher sea states (>2 m) are most probably associated, except for swell events, to medium to high winds that wipe away the small-scale variations

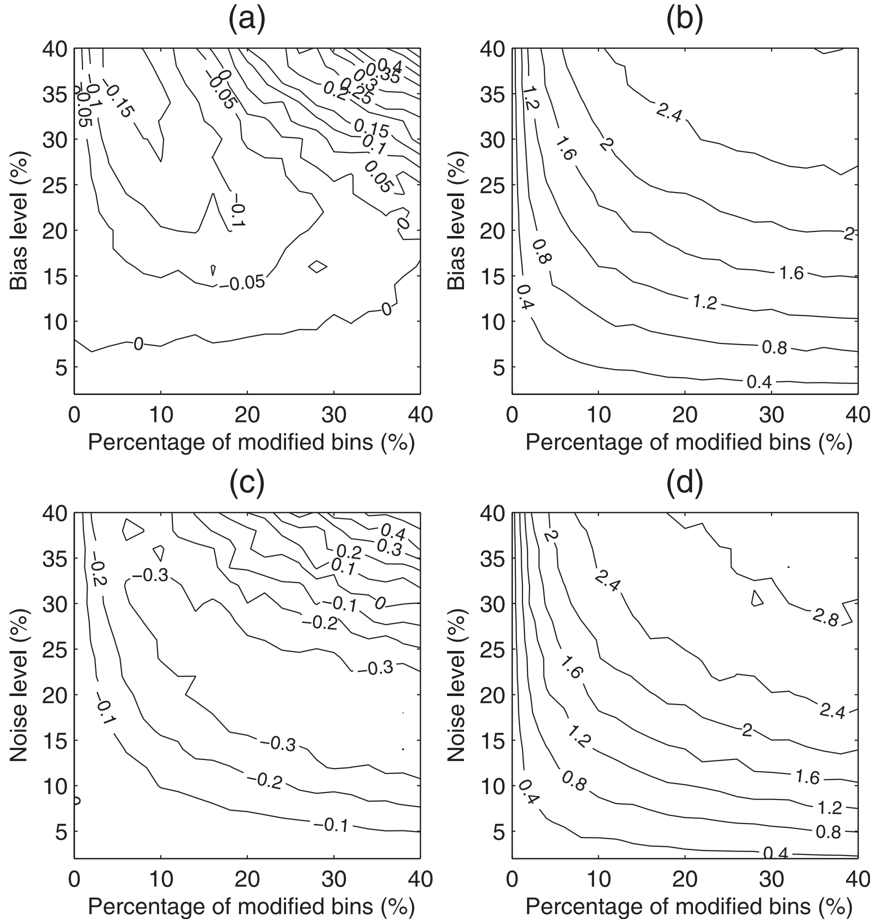


FIG. 6. (a),(c) Mean and (b),(d) rms of the difference between the inverted and original backscatter fields as a function of the percentage of modified waveform bins and noise or bias level for the (a),(b) constant bias cases and (c),(d) Gaussian noise cases.

of surface backscatter. In such cases, high-resolution mapping of surface backscatter is certainly of little interest.

In practice, HR altimeter waveforms are provided by satellite mission processing centers within the so-called Sensor Geophysical Data Record (SGDR). The raw waveforms are coded over a limited number of bits and have to be rescaled using the radar Automatic Gain Control to obtain the power backscattered by the surface. We use the rescaling method presented by SSALTO (1999) for *Jason-1*. During the *Jason-1* mission, the satellite experienced major problems of mispointing. Mispointing alters the shape of the altimeter waveforms (Hayne 1980); in particular, it modifies the slope of the trailing edge [i.e., the $e^{-u/u_b}$ term of Eq. (3)] and it attenuates the signal. When mispointing is severe [i.e., when the estimate of the square of the off-nadir angle is outside the limits recommended by the Archiving, Validation, and Interpretation of Satellite Oceanographic data (AVISO) processing center ($-0.02$ deg$^2$ and 0.16 deg$^2$)], the waveforms are discarded. For lower mispointing, the waveforms are corrected using the Hayne (Hayne 1980) model; that is,

$$\sigma_{\mathrm{corr}}(t) = e^{(\zeta/\psi_b)^2}\sigma(t)e^{2\zeta^2(1+1/2\psi_b^2)}, \tag{14}$$

where $\sigma_{\mathrm{corr}}$ is the corrected waveform and $\zeta$ is the mean mispointing estimated over 5 s of measurement (to have a robust estimate of the platform mispointing). The first exponential term in Eq. (14) represents the correction of the signal attenuation and the second term shows the correction of the trailing edge slope.

## 3. Validation of the method

### *a. Constant surface backscatter*

The method is first tested using a surface of constant backscatter and constant backscatter plus a white noise

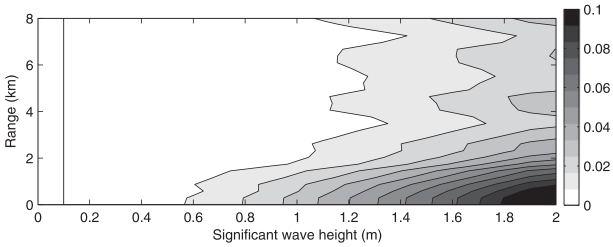


FIG. 7. Proportion of misregistration for a Jason altimeter and a 300-m-resolution surface grid as a function of swh and distance from nadir.

of 0.3-dB rms. The waveforms are computed for a Jason-like altimeter using the Brown model and a 2-m significant wave height. They are then inverted using Eq. (13). Figure 4 presents the difference between the retrieved and surface backscatter for the constant and noisy cases, and Fig. 5 presents the mean bias and rms as a function of the across-track distance. The bias is always smaller than 0.025 dB with a mean of 0.01 dB while the rms is smaller than 0.02 dB for the constant case. This shows that the inversion is unbiased and that the precision is very good. In the noisy case, the bias is always smaller than 0.05 dB with a mean of 0.03 dB and the rms is between 0.2 and 0.4 dB (i.e., of the same order of magnitude as the surface backscatter rms). Because of the sampling geometry, in particular the fact that the first telemetry sample is a disk and not an annulus, the rms is larger near nadir.

### b. *Robustness of the method*

The noisy case has been further used to test the robustness of the inversion. A percentage (from 2% to 40%) of the bins of the modeled waveforms is randomly selected and a Gaussian noise or a constant bias is then added to these selected bins. The inversion method is then applied to the modified waveforms and the mean and rms difference compared to the original backscatter field are computed as the function of the percentage of modified bins and of the noise/bias level (in percentage of the maximum amplitude of the waveforms). Figure 6 presents the mean and rms of the difference between the inverted and original fields for the constant and Gaussian noises. The results show that the bias of the inversion is always smaller than 0.5 dB. As expected, the rms increases with both the noise level and the percentage of modified bins, but remains reasonably low (<1.2 dB) for low noise level (<10%) even for large proportions of modified bins and for low percentage (<10%) of modified bins up to high noise level (<30%). The inversion method is thus effective and is almost unbiased even if a large proportion of the data is biased, and robust as the rms of the error remains acceptable even when quite a large proportion of data is biased or noised.

### c. *Effect of significant wave height*

The waveform model used in Eq. (5) neglects the elevation of the sea surface. An elevation of the surface (i.e., a change of range) corresponds to a displacement in the waveform space; an elevation of 1 m corresponds to a change of two telemetry bins. It is thus assumed that the misregistration of surface elements in the waveform space caused by elevation is negligible for low sea state at the resolution of the surface grid used for the inversion. To assess the method it is thus necessary to estimate the error induced by this hypothesis. The simplest way is to estimate the proportion of misregistration for each grid cell as a function of significant wave height. This is done by simulating the sea surface for a given wave spectrum following the method presented by Hauser et al. (2001) at a resolution significantly higher than the surface backscatter grid (here 10 m), by computing the range of each of the surface elements, and then by determining for each surface grid cell the proportion of the high-resolution surface elements whose range lies outside the range limits that can be expected if the sea surface were flat (see Fig. 3b).

The surface simulation comprises the following steps:

(i) generation of a random sample of a variable to simulate a Gaussian white noise, with mean 0 and variance 1
(ii) computation of the Fourier transform $B(k_x, k_y)$ of this noise, which has the property that its phases are uniformly distributed between 0 and $2\pi$
(iii) multiplication of this normalized noise spectrum by the directional wave energy spectrum $F$ to obtain a complex spectrum $S_p(k_x, k_y)$:

$$S_p(k_x, k_y) = \sqrt{F(k_x, k_y)}\frac{B(k_x, k_y)}{\|B\|} \tag{15}$$

(iv) computation of the inverse Fourier transform of $S_p^i(k_x, k_y)$ to provide a realization of the surface elevation for a given set of random phases

Using a Elfouhaily et al. (1997) spectrum and angular distributions, surface elevations are simulated at a 10-m resolution for significant wave height ranging from 0 to 2 m. The proportion of misregistration is then computed for the surface backscatter grid for the Jason altimeter (see Fig. 7). The results show that for significant wave height smaller than 1 m the misregistration is always negligible (<2%) and that for sea state smaller than 2 m it is significant (>10%) only near nadir and rapidly decreases with the distance from nadir.

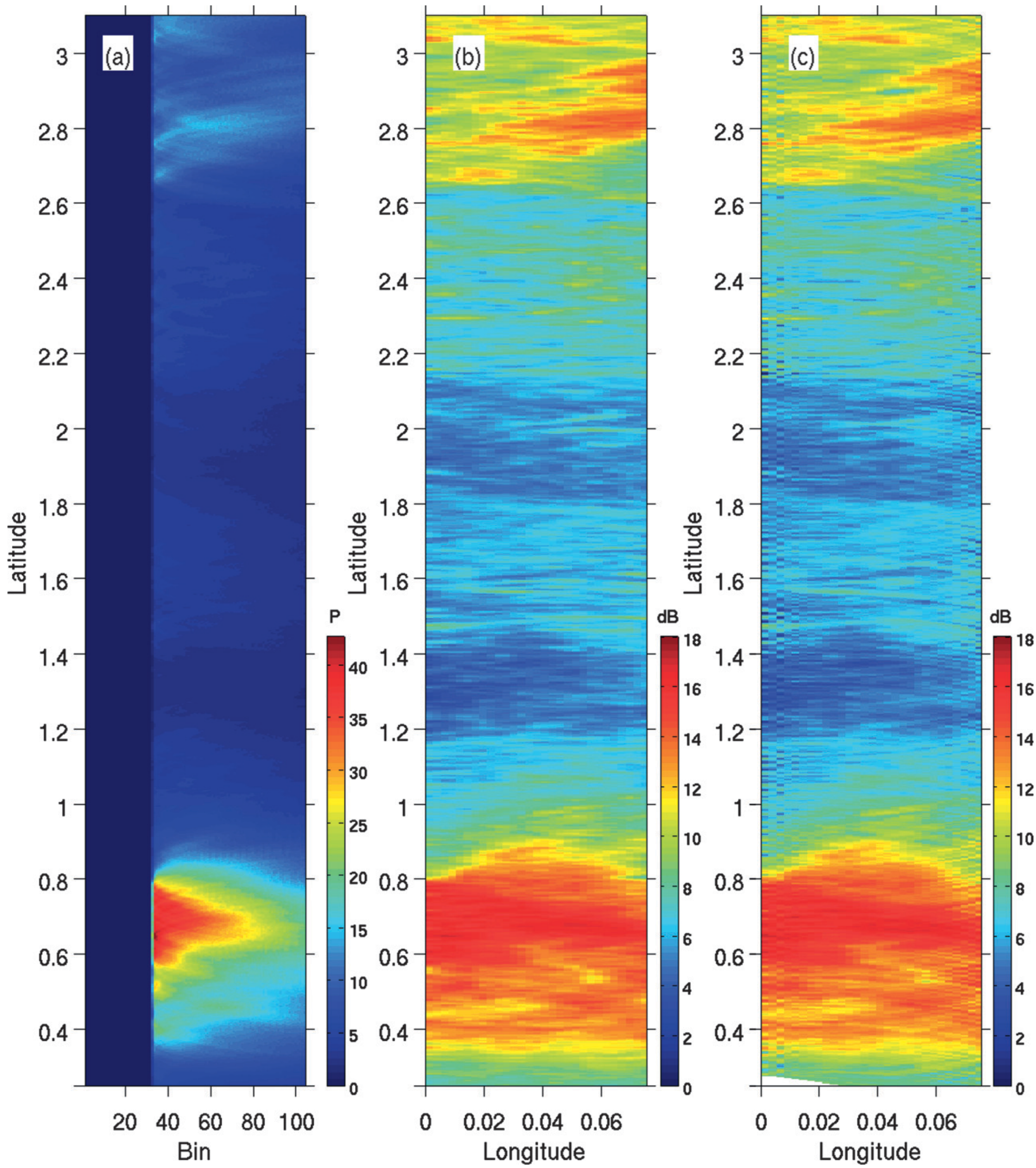


FIG. 8. (a) Modeled Jason-like altimeter waveforms, (b) surface backscatter $\sigma_0$ (dB) used to model the altimeter waveforms, and (c) surface backscatter (dB) estimated by inversion of the waveform.

*d. Modeled waveforms*

The inversion is further tested using realistic surface backscatter estimated from a SAR image under low to medium wind conditions. The Jason-like altimeter waveforms presented in Fig. 8a were computed using the SAR surface backscatter shown in Fig. 8b, the waveform model presented in Tournadre et al. (2006), and a constant significant wave height of 1 m corresponding to the mean value estimated from the SAR image spectrum.

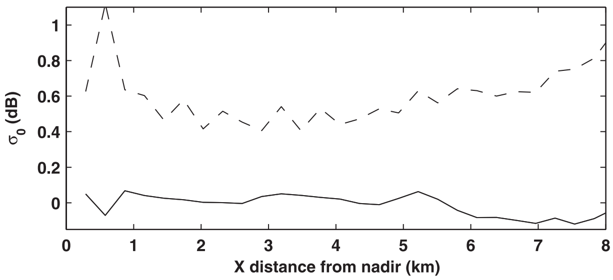


FIG. 9. Mean (solid line) and rms (dashed line) of the difference between the surface and retrieved $\sigma_0$ of Fig. 8.

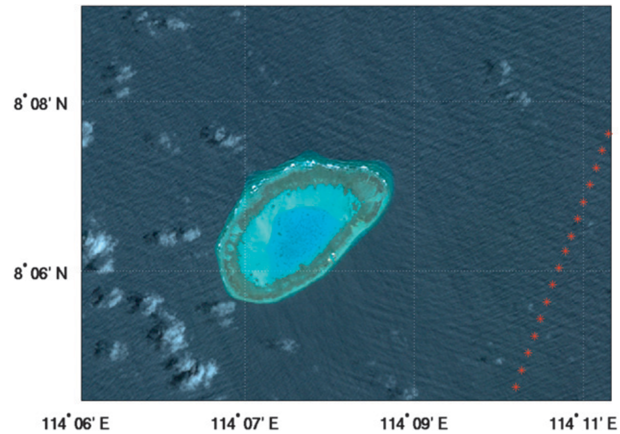


FIG. 10. Landsat 7 Thematic Mapper image of the Erica Reef. The red crosses indicate the Jason pass 51 ground track.

This $\sigma_0$ field is quite complex and presents a wide range of $\sigma_0$ as well as large, strongly reflective patches (near 0.7° and 2.7°N) and a number of slicklike features (between 1° and 2.5°N). The retrieved surface backscatter presented in Fig. 8c shows that the $\sigma_0$ field is very well reproduced and that all the patterns are present, in particular the small-scale patterns such as the slicklike features and the reflective patches. The mean bias and rms as a function of the distance from nadir are presented in Fig. 9. The bias is small at about 0.1 dB and the rms is about 0.6 dB except near nadir where it is about 1 dB.

## 4. Example of application: Modification of surface roughness by a submerged reef

Several applications of the method can be foreseen such as the analysis of rain patterns, land/sea transitions, surface slicks, lake surfaces, or small islands. An operational high-resolution backscatter altimeter product could be defined using this method for specific regions. To show the potential interest in the high-resolution backscatter fields, we choose here to focus on the analysis of the effect of a submerged reef on the sea surface roughness.

The South China Sea is punctuated by a multitude of small islands, coral reefs, and submerged reefs divided into the Spratly and Paracels groups. The Spratly group alone contains more than 600 coral reefs. Among the Spratly, Erica Reef is a small (3 km × 2 km) oval drying reef enclosing a shallow lagoon (see Fig. 10) located at 8°4′N, 114°5′E. A few drying rocks lie on its east side. The global composite 1-km bathymetry map from Sea-viewing Wide Field-of-view Sensor (SeaWiFsS) data (Stumpf et al. 2003; Robinson et al. 2000) gives a depth of less than 1 m over the reef.

The Jason satellite flies over Erica Reef for pass 51 and its ground track lies within ~3 km of the reef. The *Jason-1* HR waveforms archive from January 2002 to December 2008, that is, 255 cycles, as well as the first 40 *Jason-2* cycles from December 2008 to November 2009 were processed in terms of surface backscatter at a 290-m resolution near Erica Reef using the inversion method. Figure 11 presents the tide, the significant wave height, and the wind speed from the *Jason-1* and *Jason-2* 1-Hz Geophysical Data Record (GDR). The Jason GDR tide data are computed using the Finite Element Solution (FES2004) tide model (Lyard et al. 2006). The tide amplitude is about 1 m and the wind and wave climate is

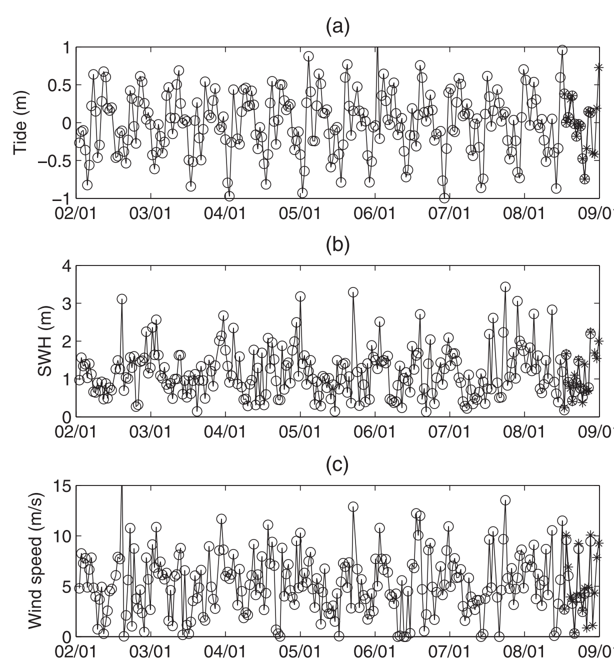


FIG. 11. (a) Tide (m), (b) swh (m), and (c) wind speed (m s$^{-1}$) near Erica Reef for the 255 *Jason-1* (circles) and 40 *Jason-2* (stars) passes from the GDR. The dates are in yy mm$^{-1}$.

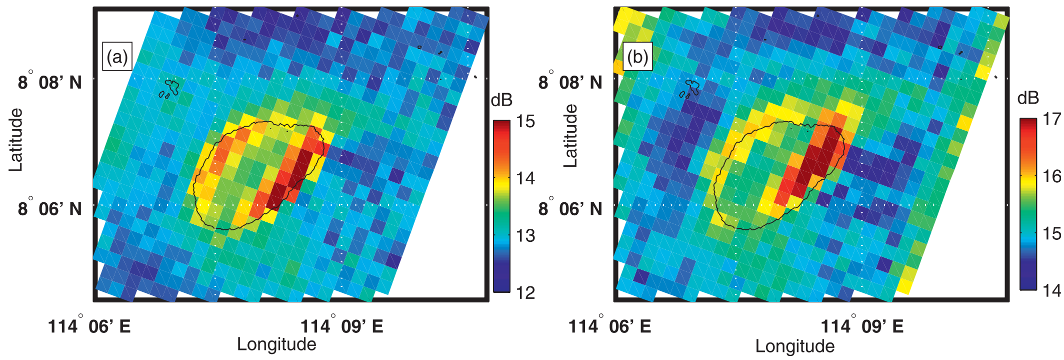


FIG. 12. (a) Mean Ku-band and (b) mean C-band surface backscatter over Erica Reef from the analysis of the *Jason-1* and *-2* waveforms. The black line represents the outline of the reef from visible imagery.

quite mild with few occurrences of swh larger than 2 m or wind speed over 10 m $s^{-1}$. To further test the method all the altimeter passes were processed, even the 12 passes corresponding to swh larger than 2 m. The results show that the method gives meaningful although noisier backscatter fields for wave height up to 3 m.

The mean Ku- and C-band backscatter presented in Fig. 12 shows the very clear signature of Erica Reef. The difference between the shallower eastern side and deeper western side is clearly visible as well as the presence of the central lagoon. The almost perfect agreement between the backscatter and the outline of the reef (black line in the figure) corroborates the inversion method and proves that the altimeter is a good imager of the ocean surface backscatter.

Interestingly, the mean backscatter over the reef (i.e., inside the black contour of Fig. 12) depends strongly on the tide as can be seen in Fig. 13. For tides lower than −40 cm, the drying of first the eastern side then the western side of the reef uncovers coral flats that are strong reflectors. This is even more clearly visible if we consider the difference $\Delta\sigma_0$ of backscatter between the reef itself and the surrounding waters, which allows us to eliminate the impact of the mean backscatter associated with wind speed. The difference is computed by subtracting from the backscatter field the mean value outside the reef, defined by the black line in Fig. 12, and within a 4-km radius. The backscatter is quite constant for tides higher than −40 cm, then strongly increases with lower tides as more coral flats are uncovered. It is worth noting that for tides from around −40 to −50 cm, that is, when the reef starts to dry, the $\Delta\sigma_0$ variability also strongly increases with larger $\Delta\sigma_0$ at lower sea states than that at higher sea states where less coral flats are uncovered. For reefs that are not very well chartered and if the tide models are to be trusted, such an analysis can help to better estimate the bathymetry at a resolution higher than that available from SeaWiFS.

Further, the dataset has been partitioned into three classes: a low-tide class (less than −40 cm) for which the reef is at least partially uncovered, and two high-tide classes from −40 to 10 cm and larger than 10 cm, where the reef is fully submerged. The mean $\Delta\sigma_0$ for each class is presented in Fig. 14. At low tides the asymmetry between the two sides of the reef confirms the difference of depth. The high backscatter observed in open water on the western side of the reef results from an artifact of the method due to the very strong quasi-specular backscatter over the coral flats. At higher tides, the reef is completely submerged and the echo from the coral flats disappears. However, the shallow depth has a very clear impact on the sea surface backscatter over the reef by modulating the roughness of the sea surface. The change of $\sigma_0$ is on the order of 1.5 dB for tides lower than 10 cm and on the order of 0.8 dB for tides larger than 10 cm.

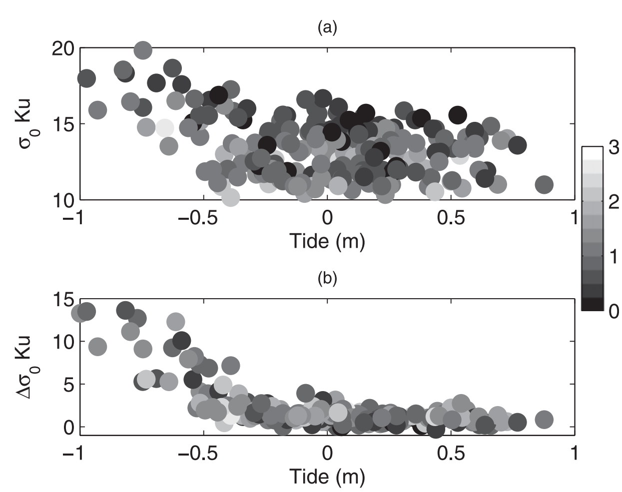


FIG. 13. (a) Mean backscatter over Erica Reef and (b) difference of backscatter between the reef and the surrounding water. The grayscale represents the swh around Erica Reef.

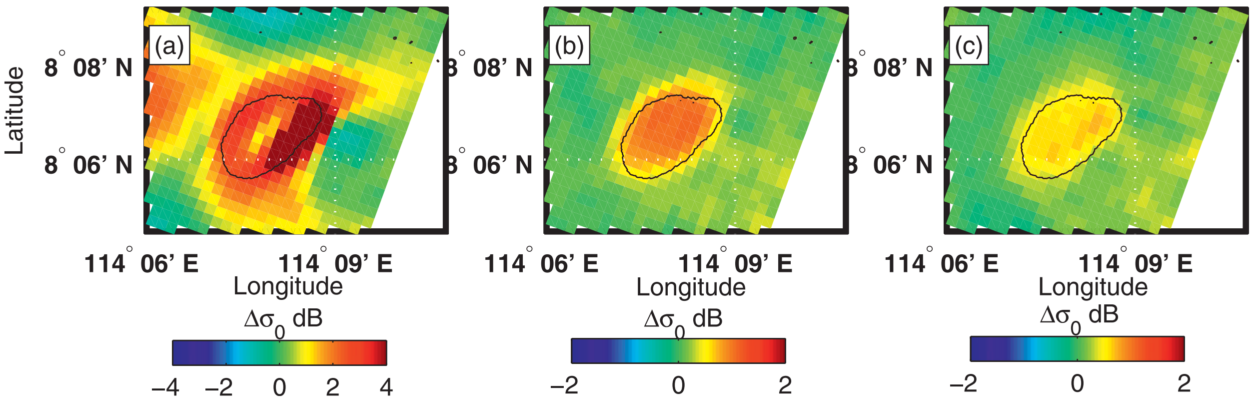


FIG. 14. Mean Ku-band backscatter variation $\Delta\sigma_0$ (a) for tides lower than −0.4 m, (b) between −0.4 and 0.1 m, and (c) larger than 0.1 m. The black line represents the outline of the reef from visible imagery.

This change certainly depends on the environmental parameters conditioning the surface roughness (i.e., sea state and wind speed). The surface backscatter is further converted to mean-square slope (mss) (Vandemark et al. 2004) to eliminate the problem of a very large fluctuation of backscatter at low wind speeds. The change of mss over the reef is then computed as the difference of mss (Δmss) between the reef itself and the surrounding

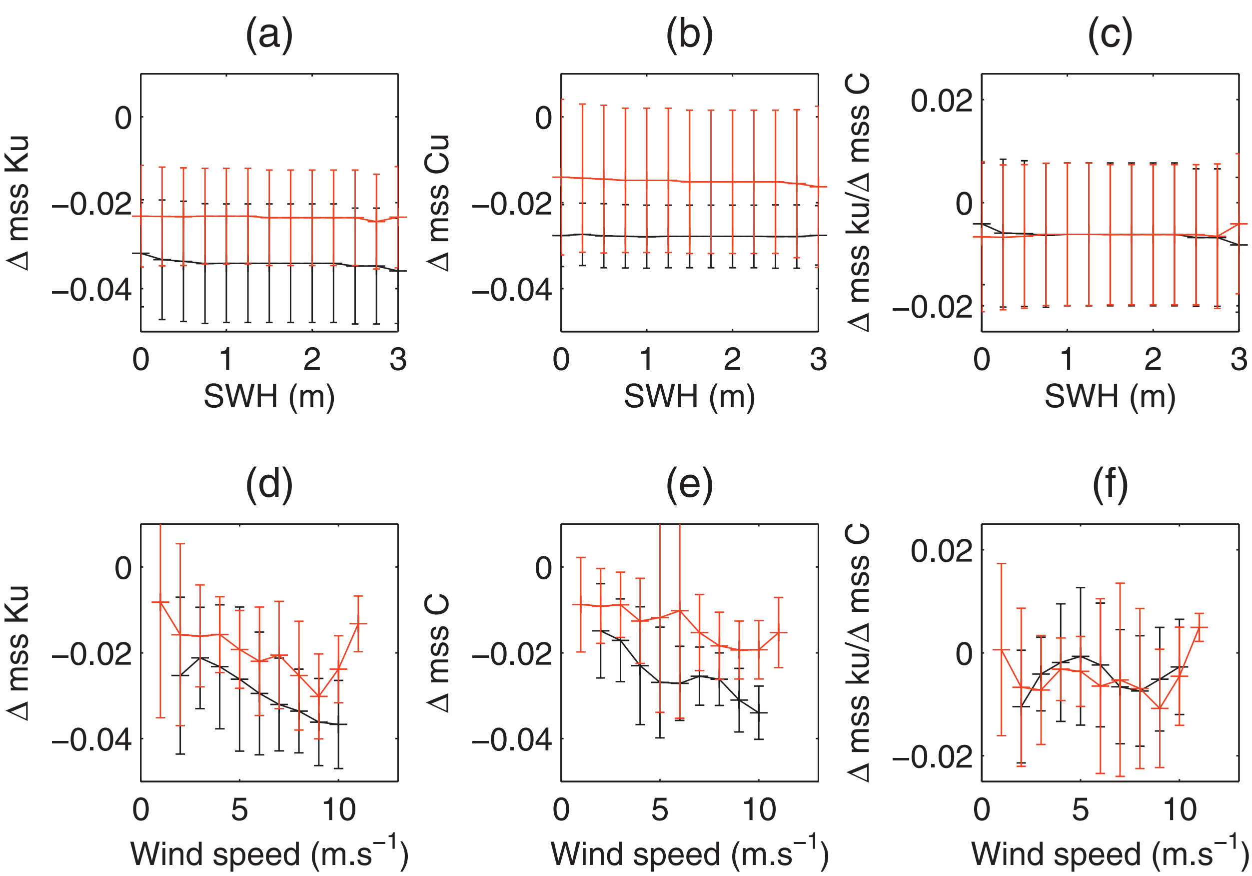


FIG. 15. Mean change of mean-square slope, Δmss, over Erica reef as a function of (a)–(c) swh and (d)–(f) wind speed for (a),(d) Ku band, (b),(e) C band, and (c),(f) the difference between Ku- and C-band mss. The red line represents the values for tides between −0.4 and 0.1 m and the black line the values for tides larger than 0.1 m.

waters. The dataset is partitioned into the two subsets corresponding to the two high-tide classes to take into account the effect of water depth.

The mean change of mss at Ku and C band as a function of swh and wind speed is presented in Fig. 15. As revealed, at both bands the mss systematically decreases over the reef by about 0.02 and 0.04 at Ku band for lower and higher tide, respectively, and 0.01 and 0.03 at C band (Figs. 15a–c). This decrease of the surface roughness over the reef is independent of the sea state. This can be interpreted as variations of the longer wave steepness (Elfouhaily et al. 1997; Gourrion et al. 2002). The contrast between airborne measurements over inland water and over sea already documented the expected impact of longer waves (Vandemark et al. 2004). The reduction of surface roughness is then found to strongly increase with wind speed for both Ku and C bands, from 0 for very low winds to 0.03 for 10 m $s^{-1}$ winds at Ku band. Within the trapped water, the longer waves cannot develop and the overall radar-detected roughness is rapidly saturating, as can be easily seen in the visible image of the reef presented in Fig. 9 where waves are no longer visible over the reef.

## 5. Conclusions

Satelliteborne radar altimeters are very powerful instruments to measure the topography of the ocean and their contributions to a better understanding of the ocean circulation are plentiful. However, up to now, very little use has been made of the high-resolution altimeter waveforms, which are also good imagers of the ocean surface backscatter. Over the ocean, a basic assumption used to model altimeter echo waveforms is to consider a homogeneous sea surface within the altimeter footprint described by a mean backscatter coefficient. When the surface backscatter varies strongly at scales smaller than the altimeter footprint size, such as in the presence of surface slicks, rain, and small islands, altimeter echoes significantly depart from the classical model and the altimeter can be interpreted as a high-resolution imaging instrument whose geometry is annular and not rectangular. A method based on the computation of the imaging matrix and its pseudoinverse to infer the surface backscatter at high resolution (~300 m) from the measured waveforms has been developed. The imaging matrix depends on the geometry of the altimeter and on the satellite orbit and can be computed for each altimeter mission. The method has been tested using synthetic waveforms for different surface backscatter fields and is shown to be unbiased and accurate.

Several applications can be foreseen to refine the analysis of rain patterns, surface slicks, and lake surfaces. We choose here to focus on the small-scale variability of backscatter induced by a submerged reef smaller than the altimeter footprint. Over Erica Reef (located in the South China Sea), 295 *Jason-1* and *-2* passes have been processed. The agreement between the inverted backscatter and the reef shows the very good high-resolution imaging capability of altimeters and the good accuracy of the method. The analysis of the change of mean-square slope over the reef as a function of tide (i.e., water depth), significant wave height, and wind speed corroborates previous results obtained by previous radar and laser wave slope observations.

*Acknowledgments.* The Collecte Localisation Satellite AVISO operation center generously supplied us with the *Jason-1* sensor geophysical data record (SGDR) necessary for this study. The authors also want to acknowledge financial support by the Centre National d'Etudes Spatiales (TOSCA program).

REFERENCES

Barrick, D., and B. Lipa, 1985: Analysis and interpretation of altimeter sea echo. *Satellite Oceanic Remote Sensing. Advances in Geophysics,* Vol. 27, Academic Press, 61–100.

Brown, G. S., 1977: The average impulse response of a rough surface and its applications. *IEEE Trans. Antennas Propag.,* **AP-25,** 67–74.

Chelton, D., J. Ries, P. Callahan, B. Haines, and L. Fu, 2001: An introduction to satellite altimetry. *Satellite Altimetry and Earth Science: A Handbook of Techniques and Applications,* L.-L. Fu and A. Cazenave, Eds., Academic Press, 1–131.

Elfouhaily, T., B. Chapron, K. Katsaros, and D. Vandemark, 1997: A unified directional spectrum for long and short wind-driven waves. *J. Geophys. Res.,* **102** (C7), 15 781–15 796.

Gourrion, J., D. Vandemark, S. Bailey, B. Chapron, C. Gommenginger, P. Challenor, and M. A. Srokosz, 2002: A two-parameter wind speed algorithm for Ku-band altimeters. *J. Atmos. Oceanic Technol.,* **19,** 2030–2048.

Hauser, D., E. Soussi, E. Thouvenot, and L. Rey, 2001: SWIMSAT: A real-aperture radar to measure directional spectra of ocean waves from space—Main characteristics and performance simulation. *J. Atmos. Oceanic Technol.,* **18,** 421–437.

Hayne, G. S., 1980: Radar altimeter mean return waveforms from near-normal-incidence ocean surface scattering. *IEEE Trans. Antennas Propag.,* **AP-28,** 687–692.

Hearn, C. J., 1999: Wave-breaking hydrodynamics within coral reef systems and the effect of changing relative sea level. *J. Geophys. Res.,* **104** (C12), 30 007–30 019.

Lyard, F., F. Lefèvre, T. Letellier, and O. Francis, 2006: Modelling the global ocean tides: A modern insight from FES2004. *Ocean Dyn.,* **56,** 394–415.

Penrose, R., 1955: A generalized inverse for matrices. *Proc. Cambridge Philos. Soc.,* **51,** 406–413.

Quartly, G. D., M. A. Srokosz, and A. C. McMillan, 2001: Analyzing altimeter artifacts: Statistical properties of ocean waveforms. *J. Atmos. Oceanic Technol.,* **18,** 2074–2091.

Robinson, J. A., G. C. Feldman, N. Kuring, B. Franz, E. Green, M. Noordeloos, and R. P. Stumpf, 2000: Data fusion in coral reef mapping: Working at multiple scales with SeaWiFS and astronaut photography. *Proc. Sixth Int. Conf. on Remote Sensing for Marine and Coastal Environments,* Vol. 2, Charleston, SC, Veridian ERIM International, 473–483.

SSALTO, 1999: Algorithm definition, accuracy and specification. Volume 2: CMA altimeter level 1B processing. Tech. Rep. SMM-ST-M2-EA-11003-CN, Centre National d'Etdudes Spatiales, Toulouse, France, 226 pp.

Stumpf, R. P., K. Holderied, J. A. Robinson, G. Feldman, and N. Kuring, 2003: Mapping water depths in clear water from space. *Coastal Zone 03, Proc. 13th Biennial Coastal Zone Conf.,* Baltimore, MD, NOAA/CSC/20322-CD, CD-ROM.

Tournadre, J., 1998: Determination of rain cell characteristics from the analysis of TOPEX altimeter echo waveforms. *J. Atmos. Oceanic Technol.,* **15,** 387–406.

——, B. Chapron, N. Reul, and D. C. Vandemark, 2006: A satellite altimeter model for ocean slick detection. *J. Geophys. Res.,* **111,** C04004, doi:10.1029/2005JC003109.

Vandemark, D., B. Chapron, J. Sun, G. H. Crescenti, and H. C. Graber, 2004: Ocean wave slope observations using radar backscatter and laser altimeters. *J. Phys. Oceanogr.,* **34,** 2825–2842.